Letter

Time-Delayed Magnetic Control of X-ray Spectral Enhancement in Two-Target Nuclear Forward Scattering

Po-Han Lin,[1,†] Yu-Hung Kuan,[1,†] Yen-Yu Fu,[1] and Wen-Te Liao[1,2,3,*]

[1] *Department of Physics, National Central University, Taoyuan City 32001, Taiwan*
[2] *Physics Division, National Center for Theoretical Sciences, Taipei 10617, Taiwan*
[3] *Center for Quantum Technology, Hsinchu 30013, Taiwan*

(Received 2 November 2021; revised 13 May 2022; accepted 5 October 2022; published 4 November 2022)

Hard-x-ray spectral redistributions using single or multiple magnetic switching in two-target nuclear forward scattering is theoretically studied. We show that our system is noncommutative, namely, a magnetic perturbation at the downstream target leads to a higher spectral intensity enhancement than the spectral boost by a magnetic perturbation at the upstream target. Our scheme not only enhances the spectral intensity to tenfold but also provides a time-delayed magnetic control on the Fano-like spectrum. The present two-target results pave the way towards a brighter and more flexible x-ray source than the one-target scheme for precision spectroscopy of nuclear resonances utilizing modern synchrotron radiation.

DOI: 10.1103/PhysRevApplied.18.L051001

Dynamic perturbations on nuclear resonant scattering of x rays has a long history starting from the pioneering work [1] and lead to the alternation of x-ray frequency and time spectrum [2–36]. These perturbations are implemented by either mechanical vibrations [1,5,20,29,33,37–40] or magnetic switching [6–9,13–17,19]. Coherent control of hard x rays also inspires many theoretical proposals in fundamental physics [41–44] and for information technology [25,27,30,35,45]. Moreover, spectral enhancement of x-ray synchrotron radiation pulses in nuclear forward scattering (NFS) had been observed with the time discrimination between the scattered signal and the input [11,21]. The enhancement can also be achieved by a sophisticated control over the target trajectory without the temporal discrimination [33]. The underlying physics of the latter is the spatial phase shift due to the abrupt target motion [12], which leads to Fano resonance [33,46,47], namely, the interference between the incident broadband synchrotron radiation and the nuclear resonant scattering. This can transfer off-resonant photons onto the tiny resonant fraction and leads to the spectral enhancement. Here, we theoretically show that the magnetic switching, used in many pioneering works [16,18,19], in either single- or two-target NFS system also results in the Fano spectral enhancement. In contrast to the mechanical control, our scheme invokes the sign reversal of the nuclear Zeeman energy [16,18,19,27]. One can observe some similarities between our two-target system and the pioneering works [6,8,16] using a narrowband radioactive x-ray source. The use of broadband synchrotron radiation in our case renders Fano resonance and the spectral enhancement possible. We find the noncommutativity [38,39], i.e., inverting either magnetic fields in two-target system [16,27] leads to different spectral enhancements. We also demonstrate the time-delayed magnetic control on the Fano-like spectrum [46,47]. Our scheme potentially leads to a bright synchrotron Mössbauer source [48–55] and sensing applications [47,56].

Figure 1(a) illustrates the two-target NFS system, and Figs. 1(b) and 1(c) depict the ^{57}Fe nuclear-level scheme [19,27]. Two ^{57}Fe isotopically enriched $^{57}FeBO_3$ crystals are impinged by a linearly polarized x ray of 14.4-keV photon energy. The incident x ray drives $|1\rangle \to |3\rangle$ and $|2\rangle \to |4\rangle$ transitions. Here m is the nuclear spin projection along the z axis. Δ_g and Δ_e are the hyperfine splitting for ground states and excited states, respectively. When applying external magnetic fields $\vec{B}_1$ and $\vec{B}_2$ of few tens of gauss in the easy plane of a $^{57}FeBO_3$ crystal, the orientation of the crystal magnetization can be easily switched by inverting each magnetic field within a few ns (the red upward arrows become the downward arrows) [19].

When turning over the magnetic field, the energy levels will exchange as demonstrated by Fig. 1(c) [16,18]. As illustrated in Fig. 1(d), in a two-target NFS system one can switch $\vec{B}_1$ at $t = \tau_1$ and $\vec{B}_2$ at $t = \tau_2$ with a time delay $\tau_D = \tau_2 - \tau_1$. We show that such time-delayed magnetic control leads to versatile manipulations of the NFS frequency spectrum.

The following optical-Bloch equation (OBE) describes our two-target NFS system [23,24,27,35,44,45,57,58]:

*wente.liao@g.ncu.edu.tw
†These authors contributed equally to this work.

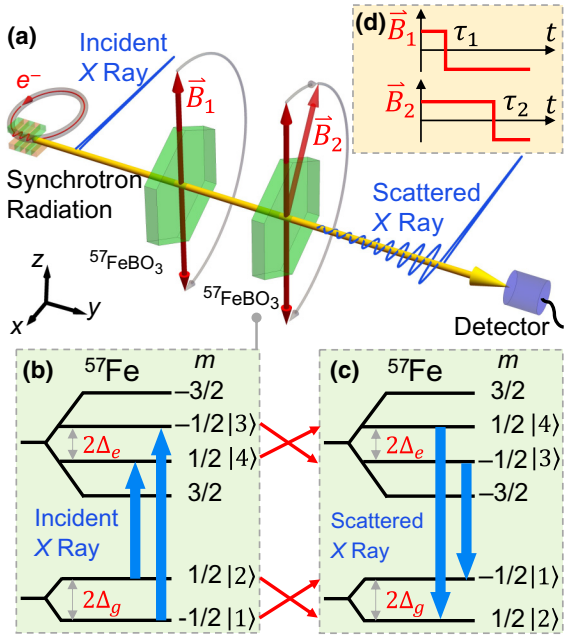

FIG. 1. (a) A linearly polarized x-ray synchrotron radiation of 14.4 keV (blue curves) impinges on two $^{57}FeBO_3$ crystals (green hexagon) applied with external magnetic field $\vec{B}_1$ and $\vec{B}_2$ (red arrows). (b) ^{57}Fe nuclear energy level with ground (excited) state Zeeman shift Δ_g (Δ_e). The nuclear spin projection on the z axis is denoted by m. The x ray drives $|1\rangle \to |3\rangle$ and $|2\rangle \to |4\rangle$ transitions. By turning over the magnetic field $\vec{B} \to -\vec{B}$, the energy levels are shifted as illustrated in (c). (d) $\vec{B}_1$ and $\vec{B}_2$ are inverted at $t = \tau_1$ and $t = \tau_2$, respectively, with a time delay $\tau_D = \tau_2 - \tau_1$.

$$\partial_t \rho_{31}^{(j)} = -\left[\frac{\Gamma}{2} + i\Delta M_j(t)\right]\rho_{31}^{(j)} + i\frac{a}{4}\Omega_j, \quad (1)$$

$$\partial_t \rho_{42}^{(j)} = -\left[\frac{\Gamma}{2} - i\Delta M_j(t)\right]\rho_{42}^{(j)} + i\frac{a}{4}\Omega_j, \quad (2)$$

$$\frac{1}{c}\partial_t \Omega_j + \partial_y \Omega_j = i\eta_j(\rho_{31}^{(j)} + \rho_{42}^{(j)}) - \frac{k}{2i}(n^2 - 1)\Omega_j. \quad (3)$$

Here index $j \in \{1, 2\}$ indicates the quantity for the jth target. $\Omega_j = \Pi E_j/\hbar$ is the x-ray Rabi frequency, where E_j is the x-ray electric field strength, Π the nuclear transition dipole moment, and $\hbar$ the reduced Planck constant. $\rho_{31}^{(j)}$ and $\rho_{42}^{(j)}$ are the quantum coherence of $|1\rangle \to |3\rangle$ and $|2\rangle \to |4\rangle$ transitions in Fig. 1(b), respectively. $\Gamma = 1/141$ GHz is the spontaneous decay rate of excited states $|3\rangle$ and $|4\rangle$, and $\Delta = \Delta_g + \Delta_e$ the total Zeeman shift. The switching function $M_j(t) = -\tanh\left[(t - \tau_j)/(0.25t_d)\right]$ describes that the external magnetic field $\vec{B}_j$ is inverted at $t = \tau_j$ within a switching time of $t_d = 5$ ns. c is the speed of light in vacuum, $\eta_j = 4\Gamma\xi_j/(aL)$, and ξ_j is the nuclear resonant thickness of the jth target. $a = \sqrt{2/3}$ is the Clebsch-Gordan coefficients, and L is the sample thickness. k is the x-ray wave number, and $n \approx 1 + i9.13 \times 10^{-8}$ is the x-ray refractive index of a $^{57}FeBO_3$ crystal contributed by electrons [59–61]. The initial and boundary conditions are $\rho_{31}^{(j)}(y, 0) = \rho_{42}^{(j)}(y, 0) = \Omega_j(y, 0) = 0$, $\Omega_1(0, t) = \exp\left[-(t - t_0)^2/\tau^2\right]$, and $\Omega_2(0, t) = \Omega_1(L, t)$, where $(t_0, \tau) = (0.67\text{ ns}, 0.1\text{ ns})$. Given Ω_j is proportional to the x-ray field propagating through and emanating from the crystals, the normalized output frequency spectrum $S_j(\omega)$ is calculated by

$$S_j(\omega) = \frac{|\int_0^\infty \Omega_j(L, t)e^{i\omega t}dt|^2}{\max|\int_0^\infty \Omega_1(0, t)e^{i\omega t}dt|^2}. \quad (4)$$

When an ultrashort pulse $\delta(t)$ illuminates a two-target system with $\Delta > \Gamma$, the scattered field [23,62] is the real part of

$$E_2(t) = \delta(t) - W_1(t) - W_2(t) + \int_0^t W_2^c(t, t')W_1(t')dt'. \quad (5)$$

Here $W_j(t) = w_j(t)\exp\left[i\Delta\int_0^t M_j(\tau)d\tau\right]$ for the jth target, and $W_2^c(t, t') = w_2(t - t')\exp\left[i\varepsilon(t)\Delta\int_{t'}^t M_2(\tau)d\tau\right]$ are single-target response functions. The envelope $w_j(t) = \xi_j/\sqrt{\xi_j\Gamma t}J_1\left(2\sqrt{\xi_j\Gamma t}\right)e^{-\Gamma/2t}$ and J_1 is the Bessel function of the first kind depicting dynamical beat (DB) [4,21,27,39,58,62] and is the analytical solution of Eqs.(1)–(3) for single target [23,58,62]. Hyperfine splitting Δ induces the real part $\mathrm{Re}\left[W_j(t)\right] \propto w_j(t)\cos\left[\Delta\int_{t'}^t M_j(\tau)d\tau\right]$ term describing quantum beat (QB) [3,12,21,23,39,58,62]. The spectral enhancement can be achieved by the sign reversal either at DB or QB nodes. We introduce the exchanging function $\varepsilon(t) = M_1(t)M_2(t)$ to distinguish different x-ray radiative couplings before and after switching instant τ_j. This is different from typical NFS [21,27,39,62] and is explained later.

Four scattering paths constitute Eq. (5) [27,39,62]. $\delta(t)$ represents that no scattering occurs. $-W_j(t)$ depicts that only the jth target scatters x rays. The last convolution describes that x rays are chronologically scattered by the first target and then by the second one, and its derivation can be found in Ref. [62].

We first demonstrate the magnetic control of the single-target NFS in Fig. 2 by numerically solving Eqs. (1)–(3) and compare three kinds of magnetic switching on $S_1(\omega)$. The switching function $M_1(t)$ and output $\Omega_1(L, t)$ are illustrated in Figs. 2(a) and 2(b), respectively. Blue dashed, red dashed-dotted-filled, and black solid lines depict cases for single, 50, and without magnetic switching, respectively. In contrast to the unperturbed NFS, the perturbed nuclear dynamics experiences time reversal after each switching at QB node. This action effectively introduces a phase shift of π in the scattered x rays [19,27,35].

Figure 2(c) depicts $S_1(\omega)$ for three cases. The single switching turns two unperturbed absorption dips (black solid line) into the enhanced spectral peaks (blue dashed

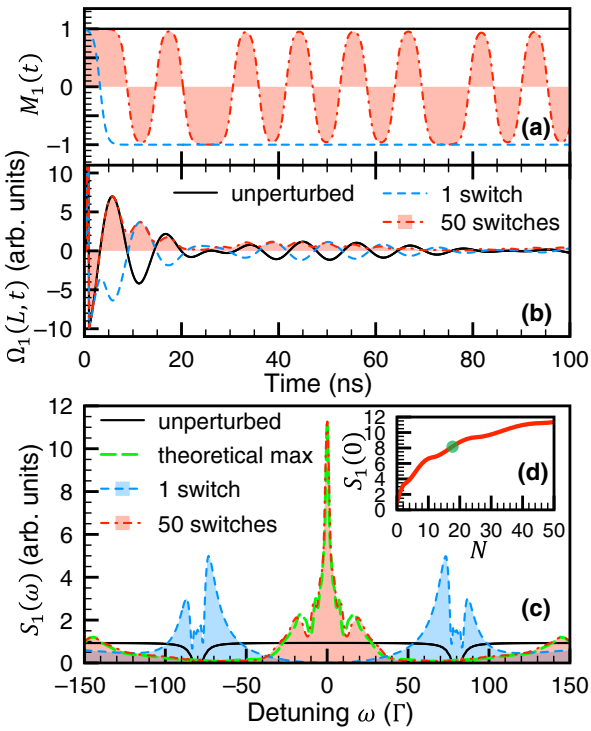

FIG. 2. Magnetic control of the single-target NFS with $(\xi_1, \Delta) = (20, 80\Gamma)$ based on Eqs. (1)–(3). (a) switching functions $M_1(t)$. (b) Output $\Omega_1(L,t)$ for single (blue dashed line), 50 (red dashed-dotted-filled line), and without (black solid line) magnetic switching. (c) Output $S_1(\omega)$. Green long-dashed line depicts the theoretic maximum spectrum. (d) Number of switching N-dependent $S_1(0)$.

line) of the maximum $S_1(\omega) = 5$ with $(\xi_1, \Delta) = (20, 80\Gamma)$. The 50 magnetic inversions eliminate the QB oscillation of $\Omega_1(L,t)$ as illustrated in Fig. 2(b) and cause an enhanced line at $\omega = 0$ and frequency doubling at $\omega = 2\Delta$ [33]. The FWHM of the central peak of the 50-switch $S_1(\omega)$ is 4Γ. $S_1(\omega)$ also approaches the theoretically optimized spectrum (green dashed-dashed-dotted line). We emphasize that the zero-frequency line is not caused by the rapid relaxation [63]. Figure 2(d) shows that $S_1(0)$ approaches the theoretic maximum of 12 when increasing the number of switchings $N \approx 50$ in 300 ns. To achieve such high repetition rate, the magnetic switching [19,25,27,36] is potentially more preferable than the mechanical vibration of a target [29,33]. Magnetic switching of a few gauss in the nanosecond time scale was experimentally realized in Refs. [6,19]. The magnetic perturbation on ^{57}Fe nuclei at a repetition rate higher than 0.1GHz was achieved in Refs. [64,65]. It deserves to mention some technical challenges of our scheme, e.g., the fast switching causes magnetoacoustic oscillations in $FeBO_3$ [14,17].

We now turn to investigate two-target NFS and show its advantages over the single-target system. Given E_2 results from multipath interference [see Eq. (5)], a two-target system renders even more flexible controls possible. In what follows we consider two identical targets with $\xi_1 = \xi_2 = \xi$.

Figure 3(a) shows the perturbed two-target $S_2(\omega)$ with $(\xi, \Delta) = (10, 80\Gamma)$ under three types of switching: (i) two magnetic fields are simultaneously inverted (green dashed-dotted line), (ii) only $\vec{B}_1$ inversion (blue dashed line), and (iii) only $\vec{B}_2$ inversion (red solid line). All spectra are the mirror image about $\omega = 0$. One can observe that each kind of switching leads to a very different spectrum. As demonstrated by the red solid-filled line, the third kind of switching not only enhances the spectral intensity by a factor of 8, but also significantly narrows FWHM of each enhanced peak. The FWHM of spectral lines at $\omega = \pm 75\Gamma$ and $\omega = \pm 85\Gamma$ is about 3.5Γ. Notably, a single $\vec{B}_2$ inversion already leads to a spectral enhancement [green dot in Fig. 3(c)] comparable to that by multiple switchings, e.g., 20 switchings, in a one-target system [the green dot in Fig. 2(d)]. In contrast to the latter, which essentially can harvest more off-resonance photons than other strongly deformed spectral lines in a single-target system [33], the former provides not only a comparable spectral boost but also an easier method for implementation than multiple perturbations. Comparing with types (i) and (iii), the overall spectral intensity of type (ii) is lower (see blue-dashed line), and there are dips touching to zero around $\omega = \pm 80\Gamma$. Figure 3(b) demonstrates the theoretical $S_2(\omega)$ based on our Eq. (5). The consistency between Figs. 3(a) and 3(b) indicates that the revised Eq. (5) can faithfully describe the perturbed two-target NFS.

Figure 3(c) illustrates the Δ-dependent peak value of the perturbed $S_2(\omega)$ for three cases. The maximum $S_2(\omega)$ saturates with 9.3, 5.3, and 3.7 for cases (iii), (i), and (ii), respectively. The rank of enhancement sustains for the variation of Δ. The tendency of increasing Δ intensifies $S_2(\omega)$ can be explained by what follows. In light of the fact that we switch a magnetic field at the first temporal QB node, shortening the QB period by increasing Δ reduces the unperturbed NFS signal prior to the switching instant and therefore raises the spectral intensity.

Moreover, not only in the frequency domain but also in the time domain, the upstream and the downstream magnetic switching results in very different output fields. Figure 3(d) illustrates the output $\Omega_2(L,t)$ from our numerical solution of Eqs. (1)–(3), where the blue dashed line denotes the type (ii) magnetic inversion, and the red solid line depicts type (iii). Notably, there is a phase shift of π between two fields for $t > 10$ ns.

Three phenomena manifest the distinction between type (ii) and (iii): the noncommutativity [38,39], the π phase difference in Fig. 3(d), and especially inverting only $\vec{B}_2$ leads to a higher spectral intensity boost than switching only $\vec{B}_1$. The above effects must result from the convolution in Eq. (5) because inverting either $\vec{B}_1$ or $\vec{B}_2$ makes W_1 and W_2 cancel each other [27]. In contrast to Ref. [39] using the two-level system to describe nucleus in

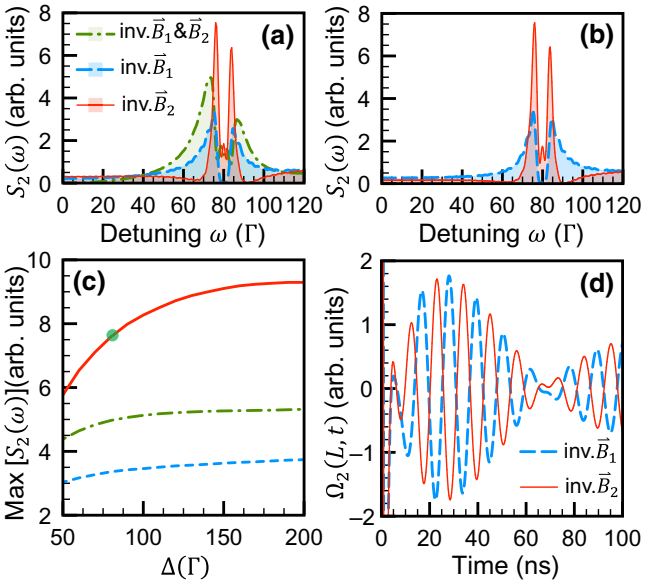

FIG. 3. Noncommutative two-target NFS frequency spectrum for $(\xi, \Delta) = (10, 80\Gamma)$. (a) $S_2(\omega)$ by numerical simulation of Eqs. (1)–(3). (b) $S_2(\omega)$ based on Eq. (5). (c) Hyperfine splitting Δ-dependent maximum $S_2(\omega)$. (d) Output $\Omega_2\,(L,t)$ by numerical simulation of Eqs. (1)–(3). Green dashed-dotted lines depict the case of switching both $\vec{B}_1$ and $\vec{B}_2$ at $\tau_1 = \tau_2 = 3.23$ ns, and the red-solid (blue-dashed) lines demonstrate the case where only $\vec{B}_2$ ($\vec{B}_1$) is inverted at τ_2 (τ_1) $= 3.34$ ns.

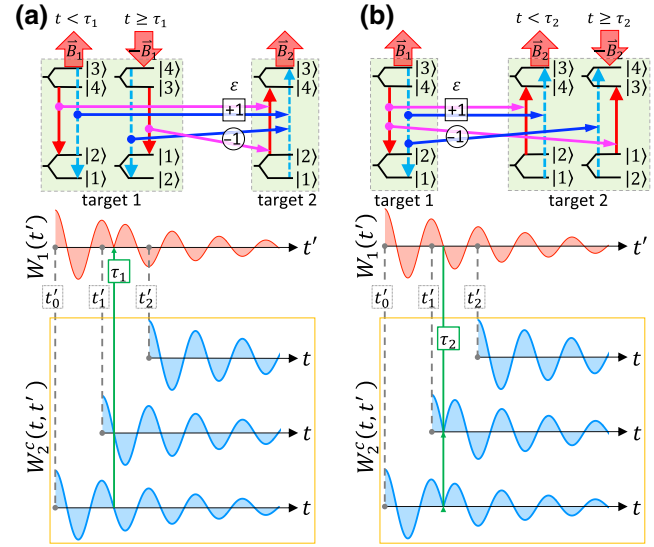

FIG. 4. Exchange of radiative coupling. (a),[(b)] shows the case where only $\vec{B}_1$ ($\vec{B}_2$) is inverted at $\tau_1(\tau_2)$. On each top panel, the exchanging function $\varepsilon = \pm 1$ denotes the radiative coupling between different transitions. Thick-red-upward (downward) arrows indicate the magnetic field before (after) switching. Thin-downward (upward) arrows depict upstream emission (downstream absorption) of x rays. Pink (blue)-rightward arrows denote x rays emitted by red- (blue-) shifted transition. On each middle panel, the red line depicts the $W_1\left(t'\right)$. On each bottom-yellow-squared panel, blue lines demonstrate $W_2^c\left(t,t'\right)$ indicated by gray-dashed lines for $t' = t'_0$, t'_1, and t'_2. Green-solid-vertical arrow highlights the switching moment.

each vibrating stainless steel, we need to consider optical coupling between nuclear hyperfine transitions of each iron borate crystal. In order to correctly calculate the convolution and theoretical spectra in Fig. 3(b), we find it is necessary to introduce the exchange of radiative coupling illustrated by Fig. 4, where (a) and (b) depict the type (ii) and (iii) switching, respectively. Given the cascade picture treating the upstream output x ray as the downstream input, the upstream nuclear transition must pair up with a downstream resonant one depending on the moment t' when x ray impinges on the second target relative to the switching instant $t = \tau_j$. Each top panel of Fig. 4 illustrates the transition pairing for exchanging function $\varepsilon = \pm 1$. Thick-red-upward and downward arrows demonstrate the magnetic field before ($t < \tau_j$) and after ($t \geq \tau_j$) switching, respectively. $\varepsilon = -1$ describes the cross-coupling that x rays emitted by the upstream demotion $|4\rangle \to |2\rangle$ ($|3\rangle \to |1\rangle$) are resonantly absorbed by the downstream transition $|1\rangle \to |3\rangle$ ($|2\rangle \to |4\rangle$). $\varepsilon = +1$ denotes the direct coupling of the identical transition. In other words, only the x ray impinging on the downstream target before the switching will experience time reversal, i.e., $W_2^c\left(t, t' < \tau_j\right) = w_2\left(t - t'\right) \exp\left[i\Delta \int_{t'}^{t} M_2\left(\tau\right) d\tau\right]$ and $W_2^c\left(t, t' \geq \tau_j\right) = w_2\left(t - t'\right) \exp\left[i\Delta\left(t - t'\right)\right]$, which are depicted by the bottom panels of Fig. 4. Our system is therefore noncommutative, and type (ii) upstream switching causes a π phase shift of $E_2\left(t > \tau_1\right)$ because $W_1\left(t' > \tau_1\right)$ contributes the minus sign in the convolution due to time reversal [see red $W_1\left(t'\right)$ curve in Fig. 4(a)]. Consequently, $E_2(t) \approx \delta(t) - \int_{\tau_1}^{t} W_2^c\left(t - t'\right) W_1\left(t'\right) dt'$ for type (ii) switching, and $E_2(t) \approx \delta(t) + \int_{\tau_2}^{t} W_2^c\left(t - t'\right) W_1\left(t'\right) dt'$ for type (iii). The positive sign results in the constructive interference between the input and the fourth scattering path, which renders inverting $\vec{B}_2$ a higher spectral intensity than switching $\vec{B}_1$.

Inspired by the noncommutativity [38,39], we investigate the type (iv) perturbation, namely, $\vec{B}_1$ or $\vec{B}_2$ are separately inverted with $\tau_D \neq 0$. Based on the interference between four paths, a fine tuning of τ_D is expected to produce a kind of interference fringe in a spectrum. Figure 5 depicts the Fano-like spectrum [46,47] $S_2\left(\omega\right)$ as a function of τ_D by numerically solving Eqs. (1)–(3) for $\xi_1 = \xi_2 = 7.5$, $\Delta = 80\Gamma$, switching $\vec{B}_1$ at $\tau_1 = 3.28$ ns, and inverting $\vec{B}_2$ at $\tau_2 = \tau_1 + \tau_D$. The perturbed $S_2(\omega)$ for $\tau_D = 4.2$ ns ($\tau_D = 6.6$ ns) is depicted by red dashed-filled line (green solid-filled line) in Fig. 5(a). Compared with the $S_2(\omega)$ of the synchronized switching in Fig. 2(b), one can transfer a four-line spectrum to a double-line $S_2(\omega)$ by the type (iv) switching. Moreover, we can control the relative height of the spectral line at $\omega = \pm 75\Gamma$ and $\omega = \pm 85\Gamma$. For $\tau_D = 4.2$ ns x-ray photons concentrate around

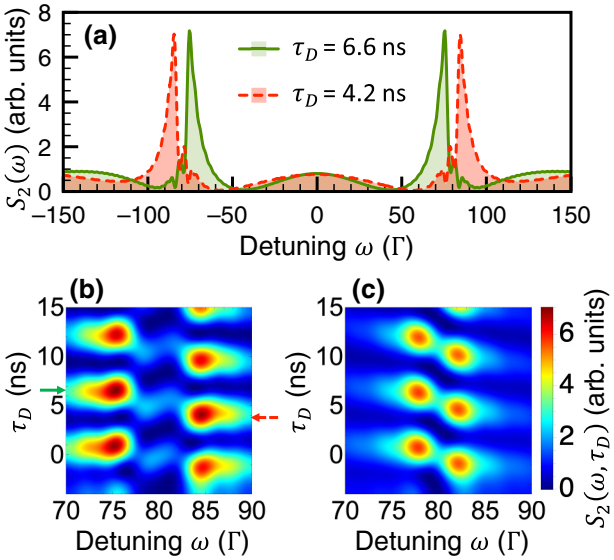

FIG. 5. Time-delayed control of Fano-like spectrum based on Eqs. (1)–(3). (a) Red dashed-filled line (green solid-filled line) is the frequency spectrum for $(\xi, \tau_1) = (7.5, 3.28$ ns) and $\tau_2 = \tau_1 + \tau_D$ where $\tau_D = 4.2$ ns (6.6 ns) indicated by the red dashed-leftward (green rightward) arrow in (b). Two-dimensional spectrogram for (b) $(\xi, \tau_1) = (7.5, 3.28$ ns), and (c) $(\xi, \tau_1) = (2.5, 3.4$ ns). (b),(c) share the same color bar, and $\Delta = 80\Gamma$ for all figures.

$\omega = \pm 85\Gamma$ with linewidth of 6Γ. A later switching of $\vec{B}_2$ with $\tau_D = 6.6$ ns inwardly redistributes NFS photons to $\omega = \pm 75\Gamma$. Figure 5(b) demonstrates the two-dimensional $S_2(\tau_D, \omega)$ for $\xi_1 = \xi_2 = 7.5$. $S_2(\tau_D, \omega)$ is a mirror image about $\omega = 0$, and so we show only the result in $90\Gamma \geq \omega \geq 70\Gamma$ for the sake of a better visualization. We observe that $S_2(\tau_D, \omega)$ is gradually and periodically modulated along the variation of τ_D. The red dashed-leftward arrow and the green-rightward arrow indicate the time delay for two cases in Fig. 5(a). In view that the tunable frequency components are determined by DB, Fig. 5(c) depicts the change of using lower resonant thickness $\xi_1 = \xi_2 = 2.5$ to relocate two controllable spectral lines at $\omega = 77.5\Gamma$ and 82.5Γ.

In conclusion, we study the magnetic controls over the x-ray frequency spectrum in two-target NFS. Our scheme results in tenfold spectral intensity enhancement with FWHM of 4Γ. This leads to a bright synchrotron Mössbauer source [48,49,52,54] for any photon flux-hungry experiments [50,52–54,54]. Our time-delayed scheme offers a selection of enhanced spectral lines, and its sharp asymmetric Fano line shape has the potential for sensing applications [47,56].

Acknowledgments.—We thank A. Pálffy, Y.-J. Chen, and D.-A. Luh for fruitful discussions. This work is supported by the Ministry of Science and Technology, Taiwan (Grant No. MOST 107-2112-M-008-007-MY3 & MOST 109-2639-M-007-002-ASP & MOST 110-2639-M-007-001-ASP & MOST 110-2112-M-008-027-MY3 & MOST 111-2923-M-008-004-MY3) and the National Science and Technology Council, Taiwan (Grant No. NSTC 111-2639-M-007-001-ASP).

[1] S. L. Ruby and D. I. Bolef, Acoustically Modulated γ Rays from Fe^{57}, Phys. Rev. Lett. **5**, 5 (1960).
[2] G. J. Perlow, Quantum Beats of Recoil-free γ Radiation, Phys. Rev. Lett. **40**, 896 (1978).
[3] G. T. Trammell and J. P. Hannon, Quantum beats from nuclei excited by synchrotron pulses, Phys. Rev. B **18**, 165 (1978).
[4] Y. Kagan, A. M. Afanas'ev, and V. G. Kohn, On excitation of isomeric nuclear states in a crystal by synchrotron radiation, J. Phys. C: Solid State Phys. **12**, 615 (1979).
[5] P. Helistö, E. Ikonen, T. Katila, and K. Riski, Coherent Transient Effects in Mössbauer Spectroscopy, Phys. Rev. Lett. **49**, 1209 (1982).
[6] G. V. Smirnov *et al.*, Nanosecond modulation of Fe^{57} Mössbauer radiation, Sov. Phys. JETP **59**, 875 (1984).
[7] E. Ikonen *et al.*, Magnetic Phase Modulation of Recoilless Gamma Radiation by Nuclear Zeeman Effect, Phys. Rev. Lett. **60**, 643 (1988).
[8] Y. V. Shvyd'ko and G. Smirnov, Experimental study of time and frequency properties of collective nuclear excitations in a single crystal (gamma-ray resonance), J. Phys.: Condens. Matter **1**, 10563 (1989).
[9] F. Vagizov, The splitting of hyperfine lines of 57 Fe nuclei in rf magnetic field, Hyperfine Interact. **61**, 1359 (1990).
[10] Y. V. Shvyd'ko *et al.*, Observation of intensified forward gamma-ray emission in spontaneous nuclear decay, JETP Lett. **53**, 69 (1991).
[11] Y. Shvyd'ko and R. Lindberg, Spatiotemporal response of crystals in x-ray Bragg diffraction, Phys. Rev. ST Accel. Beams **15**, 100702 (2012).
[12] P. Helistö, I. Tittonen, M. Lippmaa, and T. Katila, Gamma Echo, Phys. Rev. Lett. **66**, 2037 (1991).
[13] Y. V. Shvyd'ko and G. Smirnov, Enhanced yield into the radiative channel in Raman nuclear resonant forward scattering, J. Phys.: Condens. Matter **4**, 2663 (1992).
[14] Y. V. Shvyd'ko *et al.*, Nuclear diffraction of Mössbauer radiation under the influence of magnetoelastic excitation, Europhys. Lett. **19**, 723 (1992).
[15] I. Tittonen *et al.*, Observation of Mössbauer Resonance Line Splitting Caused by Rabi Oscillations, Phys. Rev. Lett. **69**, 2815 (1992).
[16] Y. V. Shvyd'ko, S. Popov, and G. Smirnov, Coherent re-emission of gamma-quanta in the forward direction after a stepwise change of the energy of nuclear excitation, J. Phys.: Condens. Matter **5**, 1557 (1993).
[17] Y. V. Shvyd'ko *et al.*, Nuclear Bragg diffraction of synchrotron radiation in the presence of acoustic vibrations, Europhys. Lett. **22**, 305 (1993).
[18] Y. Shvyd'ko *et al.*, Reversed time in Mössbauer time spectra, Phys. Rev. B **52**, R711 (1995).
[19] Y. V. Shvyd'ko *et al.*, Storage of Nuclear Excitation Energy through Magnetic Switching, Phys. Rev. Lett. **77**, 3232 (1996).
[20] G. V. Smirnov *et al.*, Nuclear Exciton Echo Produced by Ultrasound in Forward Scattering of Synchrotron Radiation, Phys. Rev. Lett. **77**, 183 (1996).

[21] Y. V. Shvyd'ko *et al.*, Hybrid beat in nuclear forward scattering of synchrotron radiation, Phys. Rev. B **57**, 3552 (1998).

[22] O. Kocharovskaya, R. Kolesov, and Y. Rostovtsev, Coherent Optical Control of Mössbauer Spectra, Phys. Rev. Lett. **82**, 3593 (1999).

[23] Y. V. Shvyd'ko, Nuclear resonant forward scattering of x rays: Time and space picture, Phys. Rev. B **59**, 9132 (1999).

[24] Y. V. Shvyd'ko, Motif: Evaluation of time spectra for nuclear forward scattering, Hyperfine Interact. **125**, 173 (2000).

[25] A. Pálffy *et al.*, Single-Photon Entanglement in the keV Regime via Coherent Control of Nuclear Forward Scattering, Phys. Rev. Lett. **103**, 017401 (2009).

[26] R. Röhlsberger, H. C. Wille, K. Schlage, and B. Sahoo, Electromagnetically induced transparency with resonant nuclei in a cavity, Nature **482**, 199 (2012).

[27] W.-T. Liao, A. Pálffy, and C. H. Keitel, Coherent Storage and Phase Modulation of Single Hard-X-Ray Photons using Nuclear Excitons, Phys. Rev. Lett. **109**, 197403 (2012).

[28] B. W. Adams *et al.*, X-ray quantum optics, J. Mod. Opt. **60**, 2 (2013).

[29] F. Vagizov *et al.*, Coherent control of the waveforms of recoilless γ-ray photons, Nature **508**, 80 (2014).

[30] W.-T. Liao and A. Pálffy, Proposed Entanglement of X-ray Nuclear Polaritons as a Potential Method for Probing Matter at the Subatomic Scale, Phys. Rev. Lett. **112**, 057401 (2014).

[31] K. P. Heeg *et al.*, Tunable Subluminal Propagation of Narrow-Band X-ray Pulses, Phys. Rev. Lett. **114**, 203601 (2015).

[32] X. Kong and A. Pálffy, Stopping Narrow-Band X-ray Pulses in Nuclear Media, Phys. Rev. Lett. **116**, 197402 (2016).

[33] K. P. Heeg *et al.*, Spectral narrowing of x-ray pulses for precision spectroscopy with nuclear resonances, Science **357**, 375 (2017).

[34] W.-T. Liao and A. Pálffy, Optomechanically induced transparency of x-rays via optical control, Sci. Rep. **7**, 321 (2017).

[35] G.-Y. Wang and W.-T. Liao, Generation of Short Hard-X-Ray Pulses of Tailored Duration using a Mössbauer Source, Phys. Rev. Appl. **10**, 014003 (2018).

[36] G. Ramien, J. Gunst, X. Kong, and A. Pálffy, X-ray-frequency modulation via periodic switching of an external magnetic field, Phys. Rev. A **97**, 063858 (2018).

[37] W. Potzel *et al.*, Investigation of radiative coupling and of enlarged decay rates of nuclear oscillators, Phys. Rev. A **63**, 043810 (2001).

[38] U. van Bürck *et al.*, Inversion of target sequence in nuclear forward scattering of synchrotron radiation, Hyperfine Interact. **141**, 151 (2002).

[39] G. V. Smirnov *et al.*, Propagation of nuclear polaritons through a two-target system: Effect of inversion of targets, Phys. Rev. A **71**, 023804 (2005).

[40] R. N. Shakhmuratov *et al.*, Single gamma-photon revival from sandwich absorbers, Phys. Rev. A **87**, 013807 (2013).

[41] W.-T. Liao, A. Pálffy, and C. H. Keitel, Nuclear coherent population transfer with x-ray laser pulses, Phys. Lett. B **705**, 134 (2011).

[42] W.-T. Liao and S. Ahrens, Gravitational and relativistic deflection of x-ray superradiance, Nat. Photonics **9**, 169 (2015).

[43] Y.-H. Kuan and W.-T. Liao, Transition between amplified spontaneous emission and superfluorescence in a longitudinally pumped medium by an x-ray free-electron-laser pulse, Phys. Rev. A **101**, 023836 (2020).

[44] Y.-H. Chen *et al.*, Transient nuclear inversion by x-ray free electron laser in a tapered x-ray waveguide, Phys. Rev. Res. **4**, L032007 (2022).

[45] X. Zhang *et al.*, Nuclear Quantum Memory and Time Sequencing of a Single γ Photon, Phys. Rev. Lett. **123**, 250504 (2019).

[46] U. Fano, Effects of configuration interaction on intensities and phase shifts, Phys. Rev. **124**, 1866 (1961).

[47] M. F. Limonov *et al.*, Fano resonances in photonics, Nat. Photonics **11**, 543 (2017).

[48] A. I. Chumakov *et al.*, Time spectra of a nearly-single-line pure nuclear reflection excited by synchrotron radiation, Phys. Rev. B **41**, 9545 (1990).

[49] G. V. Smirnov *et al.*, Synchrotron Mössbauer source, Phys. Rev. B **55**, 5811 (1997).

[50] R. Lubbers *et al.*, Density of phonon states in iron at high pressure, Science **287**, 1250 (2000).

[51] W. Sturhahn, Nuclear resonant spectroscopy, J. Phys.: Condens. Matter **16**, S497 (2004).

[52] T. Mitsui *et al.*, Development of an energy-domain ^{57}Fe-Mössbauer spectrometer using synchrotron radiation and its application to ultrahigh-pressure studies with a diamond anvil cell, J. Synchrotron Radiat. **16**, 723 (2009).

[53] T. Mitsui *et al.*, Grazing-incidence synchrotron-radiation ^{57}Fe-Mössbauer spectroscopy using a nuclear Bragg monochromator and its application to the study of magnetic thin films, J. Synchrotron Radiat. **19**, 198 (2012).

[54] V. Potapkin *et al.*, The ^{57}Fe synchrotron Mössbauer source at the ESRF, J. Synchrotron Radiat. **19**, 559 (2012).

[55] V. Potapkin *et al.*, Effect of iron oxidation state on the electrical conductivity of the Earth's lower mantle, Nat. Commun. **4**, 1 (2013).

[56] M. F. Limonov, Fano resonance for applications, Adv. Opt. Photonics **13**, 703 (2021).

[57] X. Kong, W.-T. Liao, and A. Pálffy, Field control of single x-ray photons in nuclear forward scattering, New J. Phys. **16**, 013049 (2014).

[58] W.-T. Liao, *Coherent Control of Nuclei and X-Rays* (Springer Science & Business Media, Heidelberg, 2013).

[59] *National Nuclear Data Center*, https://www.nndc.bnl.gov/ensdf/.

[60] *The Center for X-Ray Optics*, https://www.cxro.lbl.gov/.

[61] *Institute of microelectronics technology and high purity materials RAS*, http://www.iptm.ru/index.en.html.

[62] R. Röhlsberger, *Nuclear Condensed Matter Physics With Synchrotron Radiation: Basic Principles, Methodology and Applications* (Springer-Verlag, Heidelberg, 2004).

[63] A. Afanas'ev and V. Gorobchenko, Shapes of Mossbauer spectra in the rapid-relaxation limit, Zh. Eksp. Teor. Fiz **66**, 1406 (1974).

[64] L. Pfeiffer, Collapse of the magnetic hyperfine field by intense rf perturbation, J. Appl. Phys. **42**, 1725 (1971).

[65] L. Bocklage *et al.*, Spin Precession Mapping at Ferromagnetic Resonance via Nuclear Resonant Scattering of Synchrotron Radiation, Phys. Rev. Lett. **114**, 147601 (2015).